Injection schemes in THz quantum cascade lasers under operation

Franckie, Martin; Winge, David; Wacker, Andreas

Published in:
Proceedings of SPIE

DOI:
10.1117/12.2024030

2013

Invited Paper

Injection schemes in THz quantum cascade lasers under operation

M. Lindskog, D. O. Winge, and A. Wacker

ABSTRACT

The two main design schemes for Terahertz quantum cascade lasers, based on tunnelling and scattering injection, respectively, are theoretically compared. We apply our simulation package based on the non-equilibrium Green's function technique. Our results provide a good description of the gain degradation with temperature. Thermal backfilling contributes to decrease of population inversion in both cases. However, the dropping inversion cannot account for the total reduction of gain.

1. INTRODUCTION

Terahertz (THz) radiation is an important part of the electro-magnetic spectrum for high-technological applications in the fields of medicine and astronomy, amongst others.[1,2] In order to fully develop these applications, compact, high-power devices are needed and the quantum cascade laser[3] (QCL) is a promising device capable of combining these features. Much effort has been put into improving the temperature performance of these lasers, the best to date working up to 199.5 K,[4] which still requires cryostatic cooling.

The tunnelling injection (TI) design[5] has been very successful, setting new records in temperature performance repeatedly by using a diagonal lasing transition instead of a direct one.[4,6] It has not been able, however, to operate at temperatures with thermal energies significantly above the energy of the lasing transition, why it is thought that there is some fundamental limitation of the performance of QCLs of this design. It has been pointed out[7] that this limitation might come from the temperature broadening of the active QCL states making the tunnel injection to the lower laser state significant compared to the injection to the upper laser state. It is also a well known fact that thermal backfilling into the lower laser level worsens inversion at higher temperatures. Indeed, the TI design has the fundamental limitation that the population inversion cannot exceed 50 % of the total population.[8,9]

For the above given reasons, the indirect pump scheme,[8] or scattering assisted (SA) injection design was proposed, initially in the mid-infra-red, where the injection into the upper laser state is assisted by longitudinal optical (LO) phonon scattering, thus eliminating the problem of tunnel injection into the lower laser level. In addition, the population of the extractor level is supposedly lower in this design, reducing the thermal backfilling into the lower laser level. In the THz regime, SA designs[7,10,11] have operated at thermal energies exceeding the lasing energy by up to almost two times, however still at cryostatic temperatures (a maximum temperature of 163 K has been achieved[7]).

In this work we investigate the two designs described above using the non-equilibrium Green's function (NEGF) method, which gives detailed information about carrier distributions as well as current densities and gain characteristics. The stability of population inversion with respect to bias drop and temperature is studied, as well as the main reasons for the loss of population inversion and gain.

Terahertz Emitters, Receivers, and Applications IV, edited by Manijeh Razeghi, Alexei N. Baranov, John M. Zavada,
Proc. of SPIE Vol. 8846, 884603 · © 2013 SPIE · CCC code: 0277-786X/13/$18 · doi: 10.1117/12.2024030

2. MODEL

Our model was recently described in some detail[12] with the possibility to include higher harmonics of the external ac field. The model takes into account the superlattice potential, an external classical electro-magnetic field (with one dc part and one ac part), and the mean field potential from the carrier and doping densities. In addition, phonon, impurity and interface roughness scattering with electrons are included by the means of self-energies. We here briefly present our model extended to take into account the non-parabolicity of the conduction band within the effective two-band model, in which the effective Hamiltonian is written[13]

$$H = \begin{pmatrix} E_c + e\Phi & \frac{p_{cv}}{m_0}(\hat{p} - e\vec{A}) \\ \frac{p_{vc}}{m_0}(\hat{p} - e\vec{A}) & E_v + e\Phi \end{pmatrix} \tag{1}$$

and the Schrödinger equation

$$H\psi_\alpha = E_\alpha \psi_\alpha, \tag{2}$$

with the two-component wave functions

$$\psi_\alpha = \begin{pmatrix} \psi_c^\alpha \\ \psi_v^\alpha \end{pmatrix} \tag{3}$$

provides the valence band components ψ_v^α in terms of the conduction band components ψ_c^α

$$\psi_v^\alpha = -\hbar \sqrt{\frac{2m_c(E_c, z)}{E_g(z)}} \frac{1}{m_c(E_\alpha, z)} \frac{\partial \psi_c^\alpha(z)}{\partial z} \tag{4}$$

in the absence of the electro-magnetic field. Here, the effective mass is defined as

$$m_c(E, z, t) = -\frac{1}{2} m_0^2 \frac{E - E_v(z)}{|p_{cv}|^2} = m_c(E_c, z) \frac{E - E_v(z)}{E_g(z)}, \tag{5}$$

where $m_c(E_c, z)$ is the effective mass at the conduction band edge. For simplicity, we assume that the lateral effective masses are constant. Thus, we can easily obtain the valence band components from our previously used basis states $\psi_c^\alpha(z)$, to obtain the two-component basis states (3).

The two-component formalism requires new matrix elements for the desired observables and scattering terms to be calculated using the wave functions (3), which is straightforward in most cases. However, the current density can no longer be expressed simply as[12]

$$J(z, t) = e\Re\left\{ \left\langle \frac{\hat{p} - e\vec{A}}{m_c(z)} \right\rangle \right\} \tag{6}$$

since the effective mass is now energy dependent; we have to find the current operator from more basic principles, such as the continuity equation or the time derivative of the position operator, both giving the same result

$$\hat{J} = \frac{1}{A} \sum_k \sum_{mn} \begin{pmatrix} \psi_c^{n*} & \psi_v^{n*} \end{pmatrix} J(z) \begin{pmatrix} \psi_c^m \\ \psi_v^m \end{pmatrix} a_n^\dagger(\mathbf{k}) a_m(\mathbf{k}) \equiv \frac{1}{A} \sum_k \sum_{mn} J_{mn} a_n^\dagger(\mathbf{k}) a_m(\mathbf{k}), \tag{7}$$

where A is the cross-sectional area and

$$J(z) = \frac{e}{m_0} \begin{pmatrix} 0 & p_{cv} \\ p_{vc} & 0 \end{pmatrix}. \tag{8}$$

Interestingly, the current density operator, and consequently its expectation value, no longer explicitly contain the vector potential $\vec{A}$, and the basis states can be chosen to not depend on $\vec{A}$ either.

We model the QCL system by an infinite repetition of one period of the structure. This approximation allows for neglecting the leads as well as calculating the Wannier states of the sub-bands $\psi_\alpha^c(z, t)$ using periodic boundary conditions. The latter gives more reliable eigen-energies than the conventionally used Wannier-Stark

states, if sufficiently many basis states are included, while the former is hardly expected to make any difference for the central periods of THz QCLs, which typically consists of more than 200 periods.

In order to describe the system as physically accurate as possible, we use non-equilibrium Green's functions to express the observables of interest. This method, used by various groups simulating QCL systems,[14–17] keeps the coherences between the states and allows for a consistent treatment of scattering mechanisms and many-body interactions. For instance, one Green's function of interest is the lesser Green's function $G^<$, defined as:

$$G^<_{\alpha,\beta}(\mathbf{k}, t_1, t_2) = i\langle a^\dagger_\beta(\mathbf{k}, t_2) a_\alpha(\mathbf{k}, t_1)\rangle. \tag{9}$$

In order to account for non-linear response to the ac electro-magnetic field, we allow the system to oscillate at the different harmonics of the field frequency Ω. This allows for Fourier expanding in terms of the fundamental frequency Ω, yielding the Fourier transform for all self-energies and Green's functions

$$F(\mathbf{k}, t_1, t_2) = \frac{1}{2\pi}\int dE \sum_h e^{-iE(t_1-t_2)/\hbar} F_h(\mathbf{k}, E) e^{-ih\Omega t_1} \tag{10}$$

Using the above definitions, the expectation value of the current density becomes (with $t_1 = t_2 = t$)

$$\langle \hat{J}(z,t)\rangle = \frac{1}{A}\sum_k \sum_{mn} J_{mn}(z)\langle a^\dagger_n(\mathbf{k}, t) a_m(\mathbf{k}, t)\rangle \tag{11}$$

$$= -i\frac{1}{A}\sum_k \sum_{mn}\int \frac{dE}{2\pi}\sum_h J_{mn}(z) G^<_{mn,h}(\mathbf{k}, E) e^{-ih\Omega t}. \tag{12}$$

Finally, we point out that all temperatures given refer to the phonon distributions in the lattice, while the carrier distribution is in non-equilibrium.

3. RESONANT PHONON DESIGN

The tunnelling injection design has repeatedly broken the terahertz temperature record.[4,6] A resonant tunnelling current serves as a fast way of filling the upper laser state while the lower laser state is placed at an optical phonon energy above the injector state. The robust injection and very fast extraction builds up the inversion at the design bias. One period of the sample of Ref. 6 is shown in Fig. 1(a). The bias is 57 mV/period and it is around this bias that the crossing of the injector and the upper laser state (ULS) occurs. The transition energies of this design are shown in Fig. 2 as functions of applied bias. This figure shows a robust performance over a wide bias range, also seen experimentally[6] where lasing was observed over a 13 mV wide bias range per period. The injector and ULS are clinging together and the extraction energy is close to the optical phonon energy $E_{\mathrm{LO}} = 36.7$ meV in GaAs.

From the current-voltage characteristics displayed in Fig. 3(a), we see that the region of negative differential resistance (NDR) of this design begins at a bias well above the bias of the crossing of the injector and ULS in Fig. 2. This can be understood by two effects. Firstly, despite the level crossing at about 57 mV per period the densities in Fig. 1(a) show that the electrons just right of the injector well still have higher energy than those in the left one at that bias. This effect helps the system keep a positive differential resistivity and can only be seen when resolving the energy distribution of the electrons. Secondly, the aligning of the parasitic current state (PCS) to the injector and ULS also enhances the current density, which can be observed by resolving also the local current density in energy as shown in Fig. 1(b).

Another detail in Fig. 3(a) is the peak at around 37 mV per period. This has no counterpart in measurements made[6] and we currently attribute it to a long range tunnelling effect that might survive due to the lack of electron-electron scattering in our model,[12] though we have no clear cut interpretation of this phenomenon at this time. The same effect might cause an overestimate of the parasitic current from the injector and ULS to the PCS at higher biases.

As temperature increases, electrons gain thermal energy and occupy states of large in-plane momentum k to a higher degree, which results in an increase of the LO phonon emission rate in the ULS as the transition

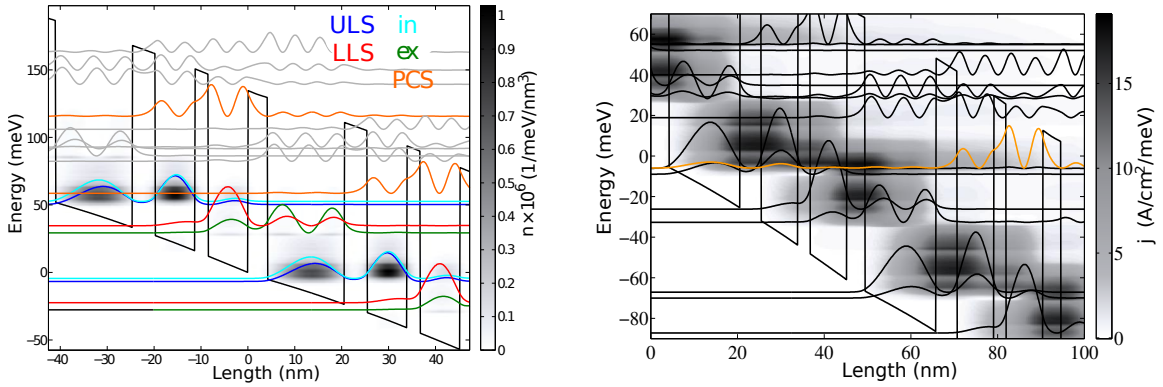

(a) (b)

Figure 1. (a) Tunnelling injection design of Ref. 6 with the upper laser state (ULS), lower laser state (LLS), injector (in) and extractor (ex) states and a parasitic current state (PCS), as well as the electron densities at a bias of 57 mV per period. (b) Energy resolved local current density at a bias of 61 mV/period, where the PCS is plotted in orange.

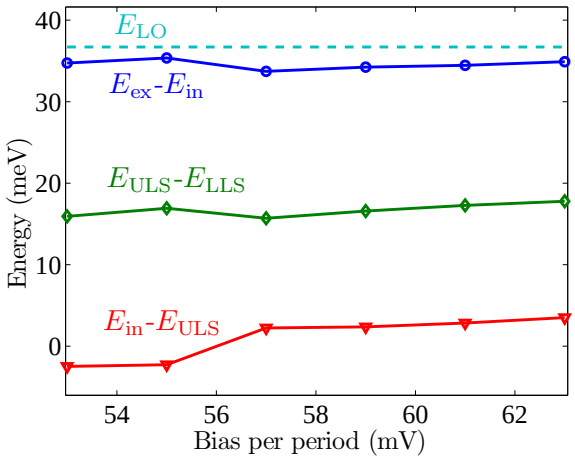

Figure 2. Transition energies for the energy levels shown in Fig. 1(a) of the tunnelling injection design as functions of applied bias. The dashed line shows the LO phonon energy E_{LO} in GaAs.

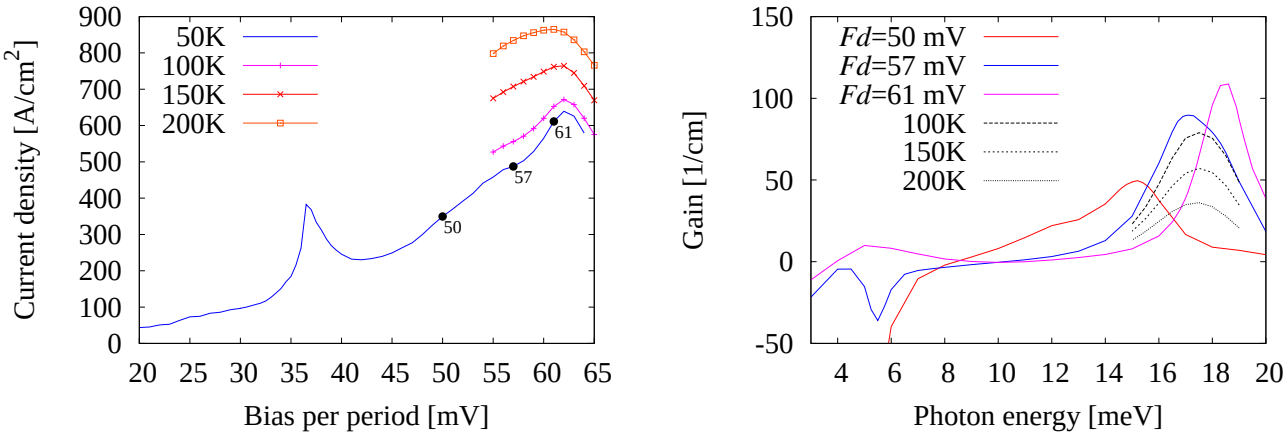

(a) (b)

Figure 3. (a) Current-voltage characteristics of the tunnelling injection design. The change in peak current density with temperature is displayed. Gain simulations were carried out at the marked bias points for 50 K, see (b). For the 57 mV per period point, gain degradation with temperature is also shown, where the dashed lines represents different temperatures.

energies $E_{\mathrm{ULS}} + E_k - E_{\mathrm{LLS}}$ and $E_{\mathrm{ULS}} + E_k - E_{\mathrm{ex}}$ of the electrons with a significant E_k are closer to E_{LO}. This explains the strong enhancement in current with temperature.

Fig. 3(b) shows the gain spectra at the bias points marked in Fig. 3(a). This shows, in addition to Fig. 2, that the lasing range is wide, since gain sufficiently large to overcome the level of losses (assumed to be significantly below 40 cm^{-1}) can be observed for a bias range of more than 13 mV per period (at 48 mV per period calculations show gain around 40 cm^{-1} for $\hbar\omega = 14$ meV). This is in good agreement with the experimental measurements of a bias range of $\sim$ 13.5 mV/period.[6]

The experimentally observed laser peak is at a photon energy of 16 meV, and a small shift in energy is also seen when going from lower to higher biases. Fig. 3(b) shows a drift of the frequency of peak gain, and at the highest current point it is substantially higher than what was measured. This might indicate that experimentally lasing has already stopped from entering the NDR, while in our simulations this has not happened due to an overestimate of the parasitic leakage current.

Our simulations show that threshold is reached at about 350 A/cm^2 which reasonably matches the experimental results. Peak current is found to be 600 A/cm^2 at 50 K, whereas measurements suggest 850 A/cm^2. However, this high current density is measured under lasing conditions, whereas the current density in Fig. 3(a) is calculated in the off-state of the laser.

As temperature increases we find that current rises and gain drops, as can be seen in Fig. 3(b) for the bias point 57 mV per period. At 200 K lattice temperature, the laser has sufficiently large gain in order to overcome the level of the losses, but this is expected to stop at a somewhat higher temperature. This is consistent with the fact that experimentally, lasing stops at 186 K heat sink temperature.[6] The degradation of inversion with temperature can be seen in Fig. 4 where the densities are plotted against temperature. Assuming a Fermi distribution for the injector state (in) we can explain half of the increase of n_{LLS} by means of thermal backfilling. Furthermore, we see no indication of a parasitic current from the injector to the LLS. A possible additional effect, which might further degrade the performance, is hot phonons out of equilibrium,[18] which is not considered here.

Despite having a drop in population inversion of about 30 % over the temperature range shown in Fig. 4, gain drops by 70 % and so the decrease in population inversion, and thus thermal backfilling, can only account for about half of the reduction of the gain. This effect was also noted in Ref. 19, and more research into the origin of the remaining reduction of gain is necessary for a complete understanding of this phenomenon.

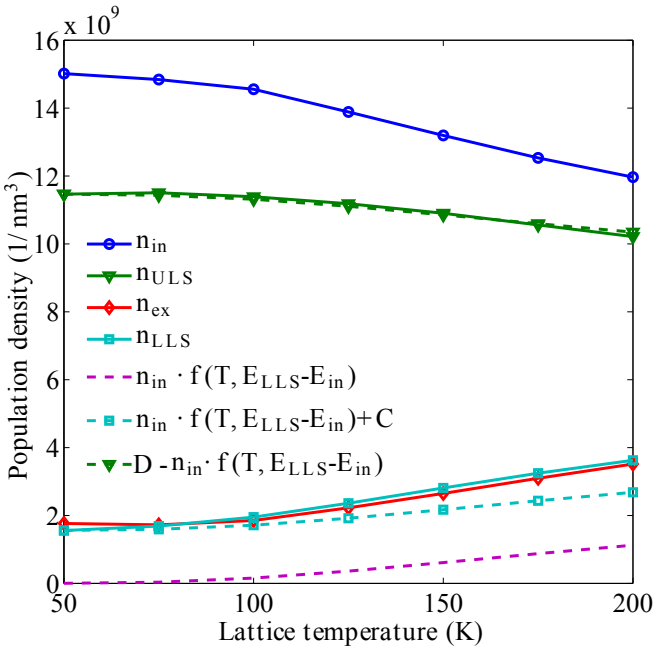

Figure 4. Temperature dependence of the densities in each state shown together with an estimate of the thermal backfilling from the injector and extractor states to the LLS as given by $n_{\text{in}} \cdot f(T, E_{\text{LLS}} - E_{\text{in}})$. The estimate is shifted by a constant C in order to coincide the curves at 200 K for easier comparison. The dashed, diamond-marked curve shows the reduction of n_{ULS} due to the backfilling of n_{LLS}, where D is again a constant used for comparing the curves. The data is taken at 57 mV/period.

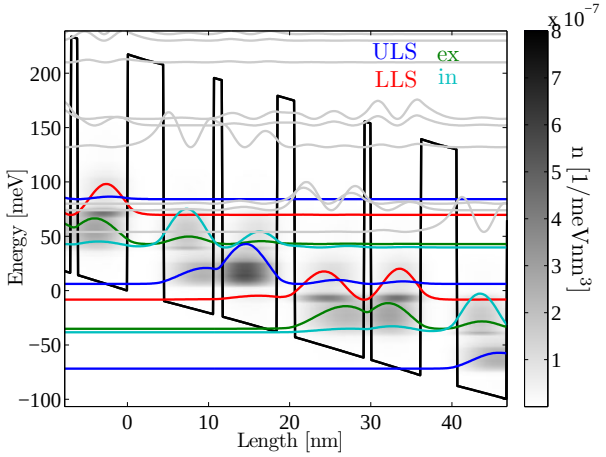

Figure 5. Band structure of the QCL in Ref. 10 as well as the carrier density and the Wannier-Stark states, at a bias of 78 mV/period for $T = 125$ K.

4. SCATTERING ASSISTED DESIGN

The scattering assisted injection scheme[8] uses an additional optical phonon transition in the current path compared to the tunnelling injection scheme, in order to inject carriers into the upper laser level. This allows for a larger bias drop over one period which is supposed to reduce thermal excitations to the lower laser level. However, one would expect there to be twice the occupation of phonon modes in the lattice, providing more lattice heating than for phonon extraction only.

We investigate here the structure, shown together with the carrier densities in Fig. 5, from Ref. 10. There we discussed the importance of taking into account the mean field in the optimization process, since even small

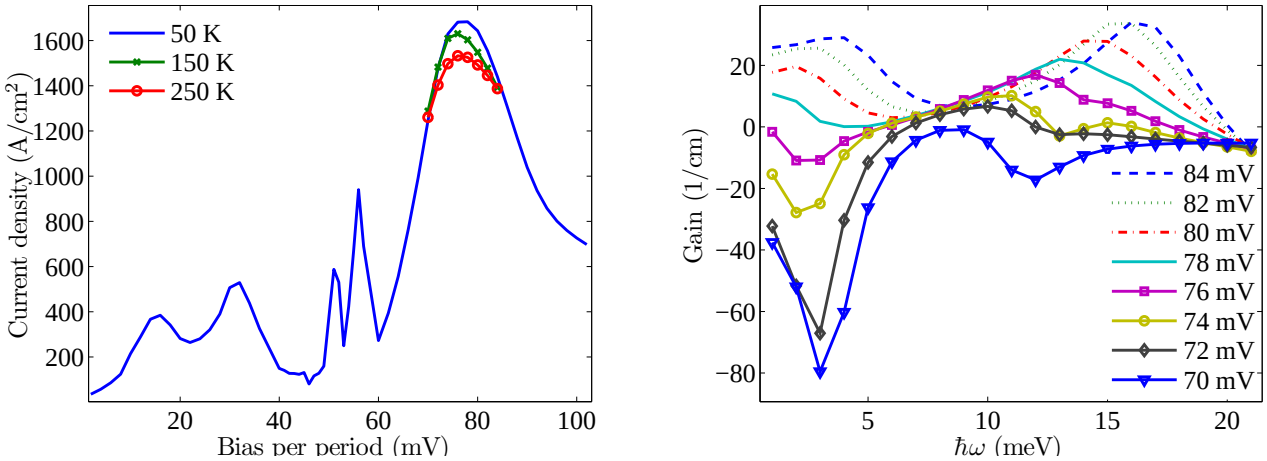

(a) (b)

Figure 6. (a) Simulated current density of the SA QCL[10] as a function of applied dc bias per period for three different lattice temperatures and (b) gain profile at different biases for the same structure, for a lattice temperature of $T = 50$ K.

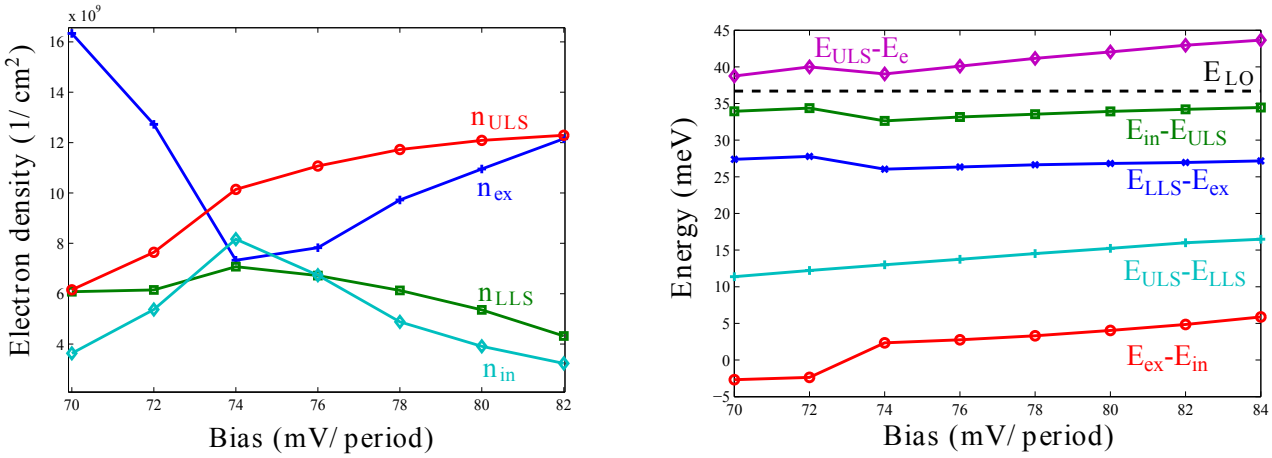

(a) (b)

Figure 7. (a) population densities of the extraction (e), injection (i), lower (LLS), and upper laser states (ULS) as well as (b) transition energies of the SA design, as functions of applied bias.

differences in the conduction band profile might put the tunnel resonance at a bias where unwanted effects occur, for instance that the phonon resonances are not satisfied.

Figure 6(a) shows the simulated current density as a function of applied bias per period. For low temperatures, the maximum current ($J_{\max}$) occurs at a bias of 78 mV/period, whereas for slightly higher temperatures it occurs at 74 mV/period, and then slowly shifts back to 78 mV/period at 300 K. There are two smaller current peaks at 16 and 32 mV/period, which arise when the injector and extractor levels align with the lower and upper laser levels respectively. These peaks are also seen in the experiment and our model reproduces them well. In addition there are two very sharp peaks at 51 and 56 mV/period, which occur due to long range tunnelling as the high energy state in the ULS well aligns with the lower and upper laser level respectively. These peaks have not been seen in experiments[10,11] and we currently attribute them to unexplained artefacts of our model. The gain, shown in figure 6(b) for different biases, exceeding the level of losses (assumed to be 20 cm^{-1}) is peaked at 12-14 meV, corresponding to frequencies of 3-3.5 THz, in good agreement with experimental data.[10]

Fig. 7(a) indicates that the tunnel resonance where $n_{\text{in}} \approx n_{\text{ex}}$ occurs around a bias of 74 mV/period. At

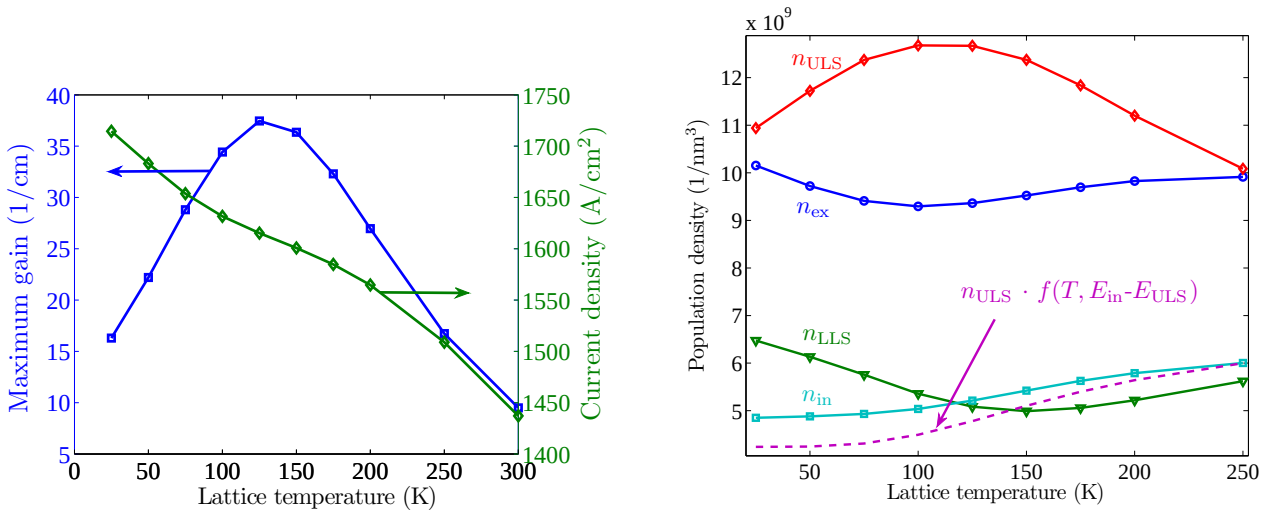

Figure 8. (a) Maximum gain and current density as well as (b) the population densities as functions of the lattice temperature at the bias of $J_{\max}$. $n_{\mathrm{ULS}} \cdot f(T, E_{\mathrm{in}} - E_{\mathrm{ULS}})$ shows the appreciated change in ULS population due to thermal backfilling into the injector state.

70 mV/period, Fig. 7(b) shows that the extraction and injection states are already near resonance and nothing drastic happens with the energy levels as the bias increases. What affects the current flow is rather that both the injection and extraction energies approach E_{LO} as the bias increases above the tunnel resonance, at roughly the same rate as the energy of the leakage transition ULS $\rightarrow$ ex increases away from E_{LO}. This ultimately leads to the peak current density $J_{\max}$ occurring at a bias of 78 mV/period, where the tunnelling rate starts to limit the current flow.

Figure 6(b) shows the gain for T=50 K and different applied biases. The gain is increasing with bias, even far into the region of NDR. We also see from figure 7(a) that inversion is increasing over the same range of biases, and that the tunnel resonance occurs at a bias of 74 mV/period. The reason is that the injection and extraction energies become better matched to E_{LO} at higher biases. Another feature of Fig. 6(b) is that there is an additional gain peak at $\hbar\omega \sim 4$ meV, prominent at high biases, coming from the population inversion between the extraction and injection states.

We see that even though a better matching of the biases where the tunnel and phonon resonances occur would increase inversion for the particular QCL studied here, the operation is not very sensitive to the detuning of the tunnel resonance, but depends more on the injection and extraction energies. Even though the NDR begins before the phonon resonances for injection and extraction are reached, this is at a 4 mV/period higher bias than the bias of the tunnel resonance. Designing the heterostructure so that the phonon resonances occur at a slightly higher bias than the tunnel resonance might therefore allow for a reliable way to delay an NDR caused by any parasitic current channel.

Turning our attention to the temperature performance we see from Figs. 8(a) and 8(b) that inversion and gain decreases with temperature above 125 K. Here the gain is lower than for the tunnelling injection structure in accordance with the worse temperature performance in the experiment. On the contrary, gain increases with temperature up to 125 K in our simulation. The reason for this increase can be attributed to the extraction energy $E_{\mathrm{LLS}} - E_{\mathrm{ex}}$ being about 10 meV lower than E_{LO}. As temperature increases, carriers in the LLS acquire more thermal energy, and at $T = 125$ K the thermal energy of $k_{\mathrm{B}}T = 10.8$ meV has exceeded the activation energy of 10 meV, and the depopulation of the lower laser state becomes more efficient than the relaxation rate from the upper to the lower laser state. This effect can be seen in Fig. 8(b) for n_{LLS} going to a minimum at 150 K and n_{ULS} a maximum at 125 K. On the contrary, the density of the injection state n_i has its minimum at $T = 25 - 50$ K, corresponding to $k_{\mathrm{B}}T \approx 2 - 4$ meV, since the injection energy only differ from E_{LO} by ~ 3 meV. Another effect that can be seen in Fig. 8(b) is the decrease of n_{ex} with temperature, indicating a

diminishing detuning of the tunnel resonance. This detuning comes from the mean field of the carriers in the LLS, and decreases as n_{LLS} decreases. Our model does not include electron-electron scattering, and in a realistic situation this scattering mechanism would likely increase the energy of the carriers in the LLS enough to allow for efficient LO phonon emission, and thus the increase of inversion and gain at low temperatures would be suppressed. At higher temperatures other scattering channels such as acoustic phonons dominate and the lack of electron-electron scattering becomes less important. At temperatures above 125 K the population of the upper laser state n_{ULS} decreases, and the population of the lower laser state n_{LLS} increases. Both the population of the injection and extraction states increase, which means the ULS loose carriers to all these states with increasing lattice temperature (the remaining states have negligible population densities).

Fig. 8(a) also shows that the current density decreases with temperature, in contrast to the TI design, as the carriers get more thermalized and the tunnelling current goes down since less current channels are available. This is also the reason for the shift of J_{max} to lower biases as temperature increases; the tunnel resonance becomes more selective as carriers get more thermalized towards the bottom of the sub-bands. This is quite the opposite to the situation for the TI QCL, where the increase in temperature opens up new current channels and the total current density increases with temperature.

In Fig. 8(b) we see that we have significant thermal backfilling from the ULS to the extraction and injection levels, even though an additional filling effect at low temperatures is necessary to fully account for the increase of n_{in}. The backfilling effect on the LLS from i is less clear due to the decrease of n_{LLS} below $T = 125$ K, however it is certainly present as a contributing factor and both thermal backfilling channels lower the population inversion of the lasing transition. This should be contrasted to the TI QCL, where thermal backfilling is filling the LLS whereas in this case it is mainly emptying the ULS. Even though thermal backfilling seem to be the most important effect preventing the QCL[10] from lasing at high temperatures, again we see that the reduction in population inversion from 125 K to 300 K of ~ 40 % cannot completely account for the reduction of gain over the same temperature range of ~ 70 %.

5. CONCLUSIONS

We have investigated the tunnelling injection and scattering assisted injection schemes for terahertz quantum cascade lasers using a model based on the non-equilibrium Green's function formalism.[12] Correct maximum current and gain peaks with respect to experiments can be reproduced, but for the TI scheme smaller pre-peaks due to long-range tunnelling in the current spectrum are grossly overestimated for reasons that are not yet clear. In contrast, for the SA scheme these pre-peaks are in good agreement with experimental data.

We conclude that thermal backfilling from the extraction to the LLS can explain about half of the decrease in population inversion with temperature for the TI scheme, while for the SA scheme it is backfilling from the ULS to the injection and extraction levels that is responsible for a large part of the decrease instead. We see no indication of other processes such as hot phonon emission or injection tunnelling directly to the LLS to have a large impact on the population inversion for the TI QCL.[6] However, thermal backfilling cannot by itself explain the reduction in gain with temperature, as was also seen in Ref. 19. We leave the question open as to what effect is responsible for further reducing the gain, be it re-absorption of carriers into higher energy levels, thermal broadening of the injection and laser levels, the thermal distributions of the population densities, or something not addressed here. Furthermore, we see that the populations of the TI QCL energy levels are less sensitive to a change in bias than those of the SA QCL, why the latter is more sensitive to placing the tunnel and LO phonon resonances at the same bias. We have also shown that parasitic (for the TI QCL) and LO phonon (for the SA QCL) current channels have a greater impact on the current flow than the tunnel resonances, something that might be utilized to avoid an early NDR.

6. ACKNOWLEDGEMENTS

This work has been partly financed by the EU FP7 project MIRIFISENS and the Swedish Research Council. The authors like to thank Emmanuel Dupont, Ghasem Razavipour and Dayan Ban for helpful discussions.

REFERENCES

[1] Tonouchi, M., "Cutting-edge terahertz technology," *Nat. Photonics* **1**(2), 97–105 (2007).

[2] Williams, B. S., "Terahertz quantum-cascade lasers," *Nature Phot.* **1**, 517 (2007).

[3] Faist, J., Capasso, F., Sivco, D. L., Sirtori, C., Hutchinson, A. L., and Cho, A. Y., "Quantum cascade laser," *Science* **264**(5158), 553–556 (1994).

[4] Fathololoumi, S., Dupont, E., Chan, C., Wasilewski, Z., Laframboise, S., Ban, D., Matyas, A., Jirauschek, C., Hu, Q., and Liu, H. C., "Terahertz quantum cascade lasers operating up to $\sim$ 200 K with optimized oscillator strength and improved injection tunneling," *Opt. Express* **20**(4), 3866–3876 (2012).

[5] Williams, B. S., Kumar, S., Callebaut, H., Hu, Q., and Reno, J. L., "Terahertz quantum-cascade laser operating up to 137 K," *Appl. Phys. Lett.* **83**(25), 5142 (2003).

[6] Kumar, S., Hu, Q., and Reno, J., "186 K operation terahertz quantum-cascade lasers based on a diagonal design," *Appl. Phys. Lett.* **94**, 131105 (2009).

[7] Kumar, S., Chan, C. W. I., Hu, Q., and Reno, J., "A 1.8 THz quantum cascade laser operating significantly above the temperature of $\hbar\omega/k_{\mathrm{B}}$," *Nat. Phys.* **7**, 3866–3876 (2011).

[8] Yamanishi, M., Fujita, K., Edamure, T., and Kan, H., "Indirect pump scheme for quantum cascade lasers: dynamics of electron-transport and very high T_0 values," *Opt. Express* **16**(25), 20748–20758 (2008).

[9] Wacker, A., "Quantum cascade laser: An emerging technology," in [*Nonlinear Laser Dynamics*], Lüdge, K., ed., Wiley-VCH, Berlin (2012).

[10] Dupont, E., Fathololoumi, S., Wasilewski, Z. R., Aers, G., Laframboise, S. R., Lindskog, M., Razavipour, S. G., Wacker, A., Ban, D., and Liu, H. C., "A phonon scattering assisted injection and extraction based terahertz quantum cascade laser," *J. Appl. Phys.* **111**, 073111 (2012).

[11] Razavipour, S. G., Dupont, E., Fathololoumi, S., Chan, C. W. I., Lindskog, M., Wasilewski, Z. R., G.Aers, Laframboise, S. R., Wacker, A., Hu, Q., Ban, D., and Liu, H. C., "An indirectly pumped terahertz quantum cascade laser with low injection coupling strength operating above 150 K," *J. Appl. Phys.* **113**, 203107 (2013).

[12] Wacker, A., Lindskog, M., and Winge, D. O., "Nonequilibrium Green's function model for simulation of quantum cascade laser devices under operating conditions," *IEEE J. Sel. Top. Quantum Electron.* **113**, 203107 (2013).

[13] Sirtori, C., Capasso, F., Faist, J., and Scandolo, S., "Nonparabolicity and a sum rule associated with bound-to-bound and bound-to-continuum intersubband transitions in quantum wells," *Phys. Rev. B* **50**, 8663 (Sep 1994).

[14] Lee, S.-C. and Wacker, A., "Nonequilibrium Green's function theory for transport and gain properties of quantum cascade structures," *Phys. Rev. B* **66**, 245314 (2002).

[15] Schmielau, T. and Pereira, M., "Nonequilibrium many body theory for quantum transport in terahertz quantum cascade lasers," *Appl. Phys. Lett.* **95**, 231111 (2009).

[16] Kubis, T., Yeh, C., Vogl, P., Benz, A., Fasching, G., and Deutsch, C., "Theory of nonequilibrium quantum transport and energy dissipation in terahertz quantum cascade lasers," *Pys. Rev. B* **79**, 195323 (2009).

[17] Haldaś and, G., Kolek, A., and Tralle, I., "Modeling of mid-infrared quantum cascade laser by means of nonequilibrium Green's functions," *IEEE J. Quantum Electron.* **47**(6), 878 (2011).

[18] Iotti, R. C., Rossi, F., Vitiello, M. S., Scamarcio, G., Mahler, L., and Tredicucci, A., "Impact of nonequilibrium phonons on the electron dynamics in terahertz quantum cascade lasers," *Applied Physics Letters* **97**(3), 033110 (2010).

[19] Nelander, R. and Wacker, A., "Temperature dependence of the gain profile for terahertz quantum cascade lasers," *Applied Physics Letters* **92**(8), 081102 (2008).